Burning on Flat Wicks at Various Orientations

Zhang, Y., Bustamante, M.J., Gollner, M.J., Sunderland, P.B., Quintiere, J.G.*

Dept. of Fire Protection Engineering, University of Maryland, College Park, MD 20742, USA
**Corresponding author email: jimq@umd.edu*

ABSTRACT

Burning on flat plates was studied at various orientations with respect to gravity. Flat wicks of ceramic (Kaowool PM) board (10 cm wide and 1 – 10 cm long) were saturated with methanol or ethanol. Steady flames were obtained that ranged from boundary layer flames to plume-type burning. The onset of unsteady flow and transition to turbulence commenced at Grashof numbers of 10^6 – 10^7, increasing with decreasing angle (towards underside burning). The average burning rate per unit area was recorded along with the flame location. Experiments on PMMA were used for comparison with the liquid-wick results. The results roughly correlated with laminar pure convective theory, and improved results were indicated when the gravity term associated with the pressure gradient normal to the plate was included. Theoretical results by the integral-method to reduce the PDE's to ODE's are presented.

KEYWORDS: Buoyancy, burning rate, combustion, flame standoff, inclined plate.

NOMENCLATURE

B	Spalding B number $\frac{Y_{o,\infty}\Delta h_c/s}{L} - \tau_o$
c	Eq. (1c)
c_p	specific heat of gas
$\overline{c_p}$	mean specific heat
Gr_l	Grashof number
Gr_l^*	modified Grashof number, $\frac{g\cos\theta L}{4\overline{c_p}T_\infty}\frac{l^3}{{\nu_\infty}^2}$
Δh_c	heat of combustion
k	thermal conductivity
l	plate length
L	heat of gasification
$\dot{m}''$	mass flow per unit area
Pr	Prandtl number, $\mu c_p/k$
Ra_l^*	modified Rayleigh number, Eq. (2b)
s	oxygen to fuel stoichiometric ratio
S	$Y_{o,\infty}/sY_{F,T}$
T	temperature
x	coordinate along plate
y	coordinate normal to plate
y_f	flame standoff distance
Y	direction with gravity vector
Y	mass fraction
Greek	
ζ_f	dimensionless flame location, Eq. (1c)
θ	angle between x and Y
μ	dynamic viscosity
ν	kinematic viscosity
Σ	Eq. (2c)
ρ	density
τ_0	$\frac{\overline{c_p}(T_w-T_\infty)}{L}$
Ω	Eq. (1b)
Subscripts	
0	initial
f	flame
F	fuel
T	condensed phase
o	oxygen
w	wall
∞	ambient
v	vaporization

INTRODUCTION

This study examines steady burning on flat plates of lengths from 1 – 10 cm long with orientations ranging from vertical ($\theta = 0°$) to horizontal, burning on the top (+) or bottom (-). While work has been performed for the purely vertical and horizontal cases, little has been done for other orientations. Early work by Blackshear and Murty [1] examined the effect of orientation for a square plate 15.9 cm ranging from horizontal bottom (θ = –90°) to top burning (θ = +90°). For that arrangement they found that the average burning rate achieved a maximum at –50º, dropping off slightly to –90º, and much more steadily to +90º. They and others [1-7] more thoroughly examined the purely horizontal or vertical orientations. Blackshear and Murty [1, 2] explained their results through the B number and the heat transfer coefficient. Kosdon and Williams [3] were the first to develop a laminar boundary layer theory for the burning of a vertical fuel surface. They noted that their prediction of the flame standoff position was about

1.5 times higher than their data. de Ris et al. [4, 5] extended their analysis to both vertical and horizontal underside burning, obtaining analytic solutions by the Pohlhausen integral method. Ahmad and Faeth [6, 7] examined both the laminar and turbulent cases following a similar theoretical approach. Investigators have conducted experiments that included the use of solid materials, ceramic plates saturated with liquid fuels, and burners to simulate real materials. Measurements on PMMA have been carried out by Ohtani et al [9] and Gollner et al [10]. More recently a direct numerical solution (DNS) of the full equations by Ali et al. [8] was obtained for a 1 cm plate at various orientations. The onset of instability from laminar flow over hot inclined plates has been reported by Lloyd and Sparrow [11] and Al-Arabi et al [12]. The current work was motivated by considering the use of burners to emulate the burning of real materials, in a non-Earth-gravity environment.

This study follows the approach by Ahmad and Faeth [6, 7], extending their work to steady burning at multiple orientations. We use their experimental technique of porous ceramic plates soaked with liquid fuels of methanol and ethanol. We also adopt their theoretical integral modeling approach. In our model, however, we add an additional term describing the role of cross flow buoyancy normal to the plate. This term is the sole buoyancy term in the ceiling burning orientation of Orloff and de Ris [5]. Except for the DNS solution of Ali et al. [8], all previous boundary layer analyses ignored this effect and only considered the buoyancy component in the flow direction parallel to the plate. This parallel component does not differentiate between top and bottom burning for the same plate angle.

EXPERIMENTAL

The experiments used ceramic wicks, as shown in Fig. 1. They were soaked with methanol or ethanol. The pyrolysis region and surrounding border were constructed of 3.2 mm thick Kaowool PM and were backed with 12.7 mm thick Kaowool 3000 to minimize heat loss to the sides and rear of the fuel laden area. Sodium silicate was applied to the interface of the plate with the border to eliminate leakage of the liquid fuel.

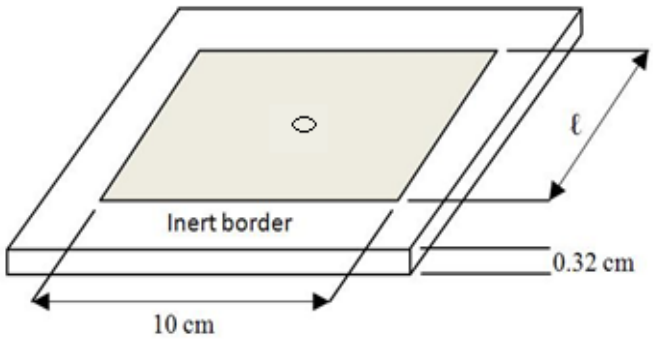

Figure 1. Sketch of a typical wick with a heat flux gauge located in the center.

10 cm wide flat wicks of length 1, 2, 3, 4, 6, 8, and 10 cm were constructed. Wicks were affixed to a stand capable of rotating 180° with respect to gravity. The mass of the wick was measured over time with a load cell, the mass-loss rate or burning rate determined by the slope of the linear mass versus time curve. The flame standoff distance was recorded during steady burning using photographs recorded parallel to the plate. The photographs were analyzed to obtain instantaneous plots over the length of the plate. Additional details of these measurements can be found in Bustamante [13], along with heat flux results for 10×10 cm methanol soaked wicks with a 3 mm Schmidt-Boelter sensor heat flux transducer located at the center of the plate.

Flame Shape

Figure 2 shows an array of instantaneous methanol flame images for the various burning orientations and plate lengths (with a fixed width of 10 cm). The images show that an increase in pyrolysis length increases fluctuations downstream of the leading edge beginning a transition to turbulence. Top burning plates show that buoyancy can cause separation of the boundary layer form the plate, resembling a plume-like flow. Beyond the plate, a wake plume occurs. For the pool fire case, the flame behavior changes from unsteady laminar flow to turbulent flow with increasing distance from the base and increased pyrolysis length. For the bottom ceiling fire case, the flame is blue and always laminar. Figure 3 shows these images in terms of digitized flame standoff locations at several instants of time when “steady average plate burning” occurred. The flame clearly begins to become unsteady at some locations.

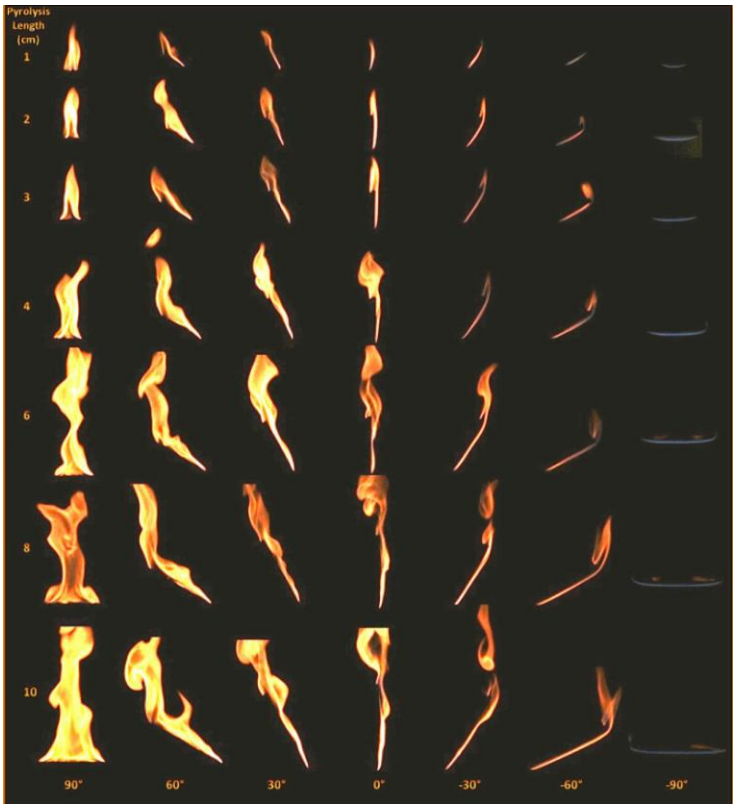

Figure 2. Methanol flame shapes at various orientations and plate (pyrolysis) lengths.

In theory, for the boundary layer flow orientations, the flame location should only be a function of the position (x) for all plate lengths. Figure 4 shows the methanol flame locations for a given angle for all of the plate lengths. In the laminar steady regions, this behavior shows the similarity of the flame location with distance. The departure from laminar flow to the onset of turbulence or plume flow is seen for the longer plates. Data for ethanol indicates that, for the laminar flows, the bottom flames are slightly thicker than the vertical or top flames.

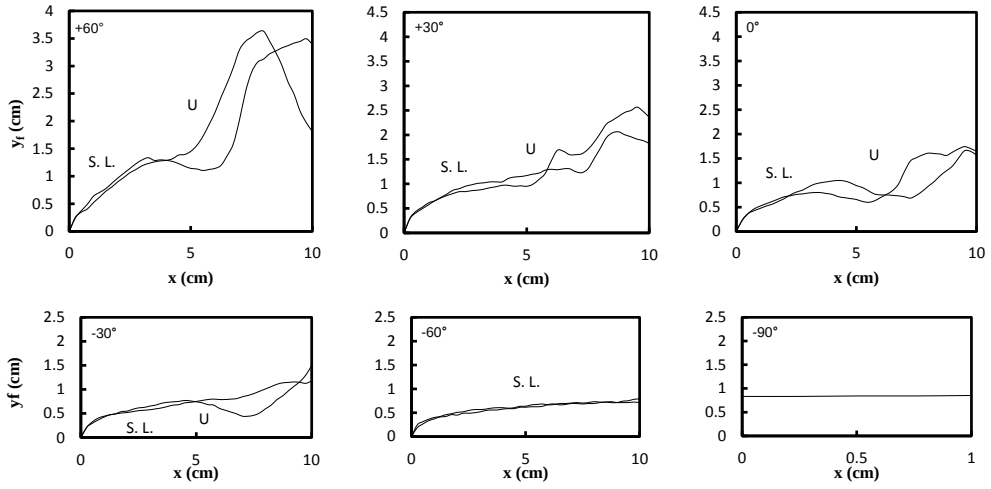

Figure 3. Measured methanol flame locations for the 10 cm long plate at all orientations. S.L. means steady laminar flow; U indicates the onset of unsteady flow. From upper left and going clockwise these are Figs. a, b, c, d, e, and f.

These data can be analyzed in terms of a Grashof number (Gr) in order to generalize the departure from steady laminar flow. The Gr at which the unsteady flow begins is seen to increase from about 10^6 to 10^7 as the orientation of burning changes from the top to the bottom of the plate, as shown in Figure 5. Predominately steady laminar flow is observed for plates at –60° and –90° for lengths up to 10 cm. For these angles, the Grashof number for transition shall be greater than 4×10^7. Some heat-transfer studies also found a decreasing Gr under which transition occurs when inclining heated surfaces of a plate from top to bottom [11, 12]. Their Gr for the end of the laminar region, however, are somewhat higher and follow a more extreme slope in comparison to this study, perhaps because they were not reacting flows which may induce an earlier transition due to large temperature gradients in the boundary layer.

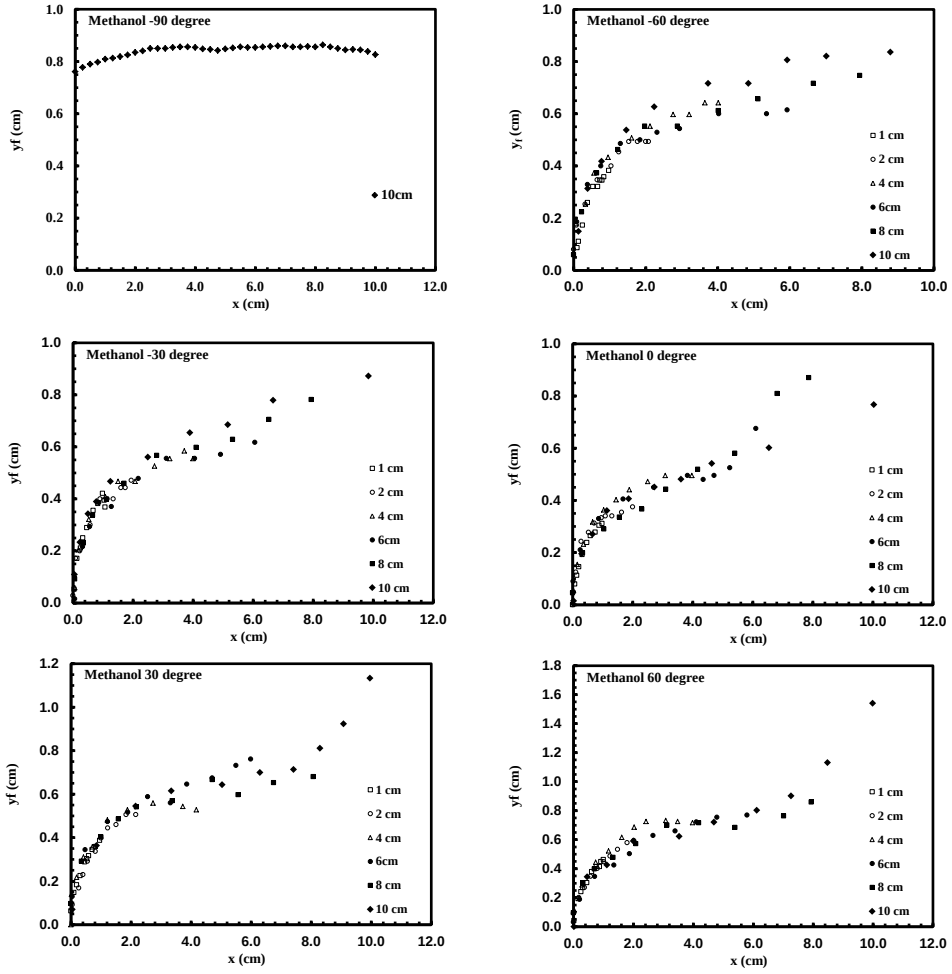

Figure 4. Methanol flame locations for all plate lengths as a function of angle.

Average Burning Rate

The average burning rate per unit area of the plate surface was determined for each plate length, orientation, and fuel. The steady values are reported, and contain some results where periodic unsteadiness occurs due to the onset of turbulence or plume-like flow. These data for all orientations and plate lengths of 1, 4, and 10 cm are shown in Fig. 6a for methanol and Fig. 6b for ethanol. As the length of the plate decreases the burning rate increases, consistent with increasingly laminar flow for shorter lengths. At very small lengths (l = 1 cm in Figure 6), the heat transfer to the plate is predominant, and therefore fuel vaporization rates significantly increase as the flame anchors close to the fuel surface over a large portion of the short length.

There is a distinct maximum at +30º (burning on the topside) for l = 1 cm, and this maximum diminishes with plate length. Blackshear and Murty [1], on the contrary, found a maximum at –50º (underside) for a plate of 15.9 cm.

Their plate length would primarily result in turbulent flows (lower burning rates), except for burning on the underside in which laminar burning would be highest, accounting for their differences.

There is little difference between the data for methanol and ethanol in this study. Figure 7 shows a more complete set of data for all lengths and orientations. The trend to larger lengths suggests why the maximum could shift from the topside to the bottom side in the data of Blackshear and Murty [1].

ANALYSIS

In order to explain the behavior of the data, the theoretical results of Ahmad and Faeth (A-F) [6, 7] are examined. As our flow is mostly laminar, with some unsteadiness, we use their laminar analytical solution. We also use their properties, as listed in Table 1. Their solution applies to boundary layer flows (-60º to +60º of our data), and accounts for the angle of inclination by the component of gravity along the plate using cosθ, but does not discriminate between top and bottom burning.

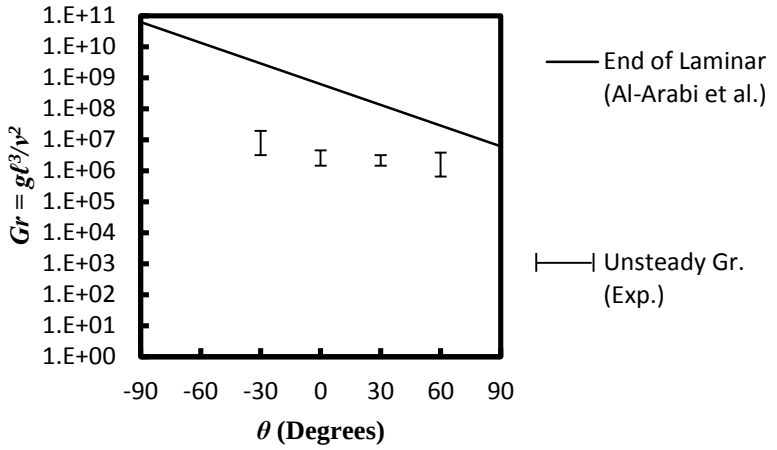

Figure 5. The Grashof number at the onset of unsteady laminar flow as a function of plate angle. The Grashof number by Al-Arabi et al. is plotted based on a flame temperature of 2200 K.

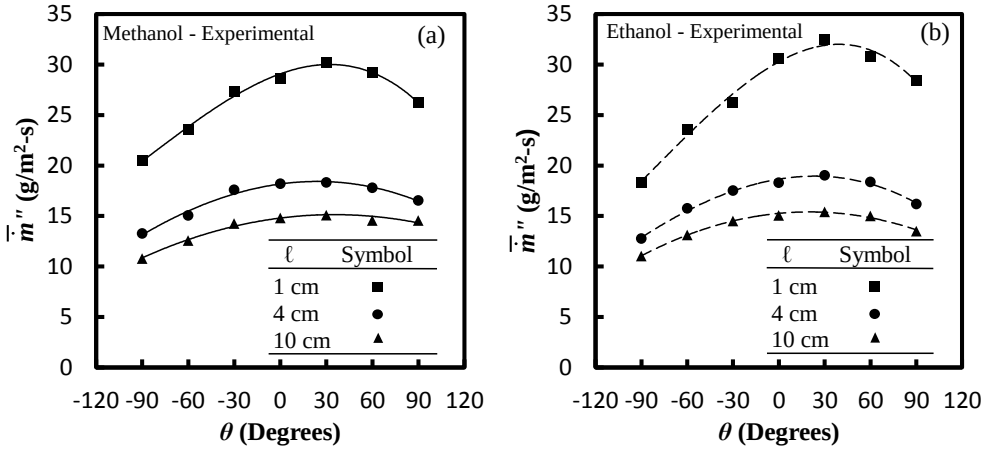

Figure 6. Burning rate per unit area as a function of orientation for plates 1, 4 and 10 cm.

Their results follow for the average flame standoff distance,

$$\left(\frac{y_f}{x}\right) Gr_x^{*1/4}\Omega = 3.6, \tag{1a}$$

where

$$\Omega = \left[\frac{BPr}{c^2\ln(1+B)}\right]^{1/2}\left[\frac{3(B+\tau_O)\zeta_f+\tau_O}{(1+B)(2+2B+Pr)}\right]^{1/4}, \tag{1b}$$

$$c \equiv \left(\frac{L}{4\overline{c_p}T_\infty}\right)\left[4(B+\tau_0)\zeta_f + B\left[\left(1-\zeta_f\right)^4 - 1\right]\right] + \zeta_f \tag{1c}$$

and

$$\zeta_f = 1 - \left[\left(\frac{B+1}{B}\right)\left(\frac{S}{S+1}\right)\right]^{1/3} \tag{1d}$$

with $S \equiv \frac{Y_{O,\infty}}{sY_{F,T}}$ and $Y_{F,T} \equiv 1$.

In the later part of this paper, it will be shown that for most non-charring materials, Ω is approximately 0.3.

The average mass burning rate per unit area is also given by A-F,

$$\overline{\dot{m}''}\ell Pr^{3/4}\Sigma Ra_\ell^{*-1/4}/\mu_\infty = 0.934\,. \tag{2a}$$

Here the number on the right-hand-side (RHS) of Eq. 2a differs slightly from the A-F [6, 7] result of 0.66, which we believe due to a computational error. The modified Rayleigh number in Eq. 2a is

Table 1. Fuel properties from Refs [6, 7]

Property	Methanol	Ethanol	PMMA
Molecular Weight (g/mol)	32.04	46.07	100
Boiling Temperature (K)	337.7	351.5	668
L (kJ/kg) [b]	1226	880	1600
c_p (kJ/kg-K) [b]	1.37	1.43	1.19
μ_{air} (x 10^{-5}) (N-s/m^2) [b]	1.8	1.8	1.8
B	2.6	3.41	1.6
s	0.154	0.111	0.21
τ_0	0.044	0.087	0.082
Pr	0.73	0.73	0.73
ζ_f [a]	0.430	0.494	0.344
$\bar{\rho}/\rho_\infty$ @ 1000 ℃	0.234	0.234	0.234
Σ	0.78	0.628	1.16
Ω	0.34	0.308	0.48

Ambient air taken to be at 298K:
ν_∞ = 15.3 x 10^{-6} m^2/s.

[a] Calculated parameter

[b] Taken at boiling point of fuel

$$Ra_\ell^* = PrGr_\ell^* = \mathrm{Pr}[\frac{Lg\ell^3\cos(\theta)}{4c_pT_\infty{\upsilon_\infty}^2}], \tag{2b}$$

where

$$\Sigma = [\frac{1+B}{B\ln(1+B)}]^{1/2}\left[\frac{1+\frac{0.5Pr}{1+B}}{3(B+\tau_O)\zeta_f+\tau_O}\right]^{1/4}. \tag{2c}$$

Full variable definitions are given in the nomenclature. The coordinate system is shown in Figure 8. In both equations 1a and 2a, the RHS should depend on the angle if there are differences between top and bottom burning.

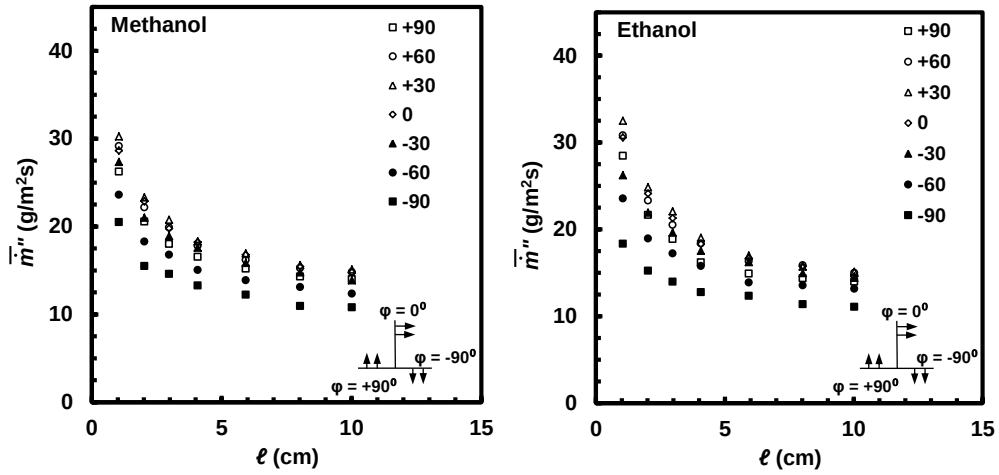

Figure 7. Average mass flux from integral model and experimental results of (a) methanol and (b) ethanol for wick lengths of 1, 2, 3, 4, 6, 8, and 10 cm at angles from -90° to +90°.

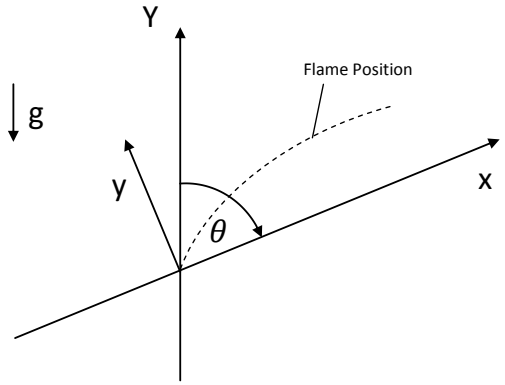

Figure 8. Coordinate system and gravity vector

The dimensionless flame standoff distance is shown in Fig. 9 according to Eq. (1). The results contain orientations of +60º (top burning) to -60º (bottom burning), for wick lengths including 1, 2, 3, 4, 6, 8, and 10 cm. The variation bars represent differences from different sample lengths (l = 1 – 10 cm). The dimensionless result should collapse the two fuels, but some difference is observed. This could be due to property effects or from neglecting radiation in the model. The correlation suggests an independence with angle within about 30%, but the theory is over twice as high. Kosdon and Williams [3] similarly found their theory over-predicted experimental flame standoff distances by about 1.5 times. Flame standoff measurements from experiments on PMMA [12] are not shown because they were based on observation of a yellow flame, not comparable to measurements in this study of the blue flame, closer to the plate surface.

The dimensionless burning rates from this study are plotted in Figure 10, along with data for 10×20 cm PMMA (20 cm pyrolysis length) by Gollner et al. [10] and 3-10 cm square sheets of PMMA by Ohtani et al. [9]. The Grashof number for the wick lengths of 1- 10 cm ranges from 10^4 to 10^7. For the 20 cm length of PMMA burning, the Grashof number is about 3×10^8, which falls within the range of transition from laminar to turbulence (10^8 – 10^{10}). Here the results indicate an increase in burning rate as the angle increases from -60º (bottom) to +60º (top burning). The two liquid fuels show this same trend, but do not collapse to within about 10%. The PMMA data, containing a mostly laminar flame over its length, also shows a similar trend with angle, but lower in magnitude. Again the theory over predicts the flame standoff distance and indicates an effect of the angle of inclination. A constant of about 0.6 would embrace most of the liquid wick data to within about 25% while ignoring the distinct trend with angle. The numerically-solved burning rate is plotted along with the experimental data. As the experimental ones,

they are solved for wick lengths of 1, 2, 3, 4, 6, 8, and 10 cm and the plotted result is the average over those multiple lengths. Adding additional cross-flow term helps to deviate the top burning from bottom burning. The numerical result almost follows the same trend as the averaged experimental data with respect to inclinations. By including the cross-flow effect, the theory yields a better prediction with respect to burning phenomena at different inclinations. These numerical results will be discussed in detail later and address the cross-flow buoyancy term neglected in the Ahmad and Faeth analytical solution.

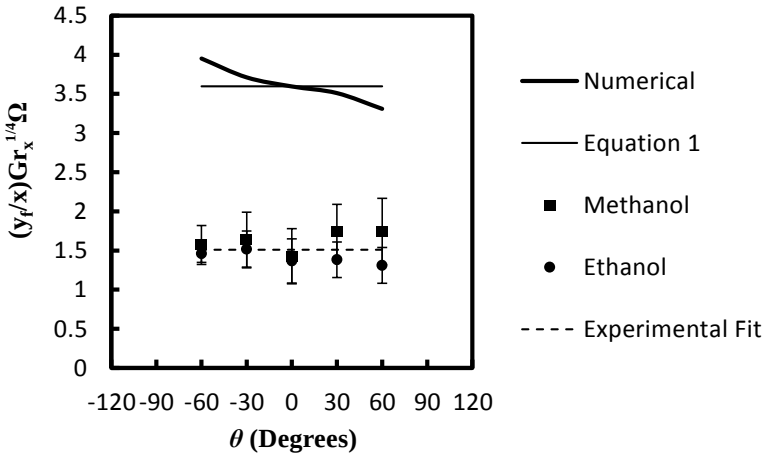

Figure 9. Dimensionless flame standoff for the full set of data. Symbols indicate average dimensionless standoff for all lengths with vertical bars indicating the variability. Equation 1 $\left(\frac{y_f}{x}\right) Gr_x^{*1/4}\,\Omega = 3.6$ is derived from Ahmad and Faeth. Numerical calculation is based on modified equations from this study and a fit of experimental data is shown.

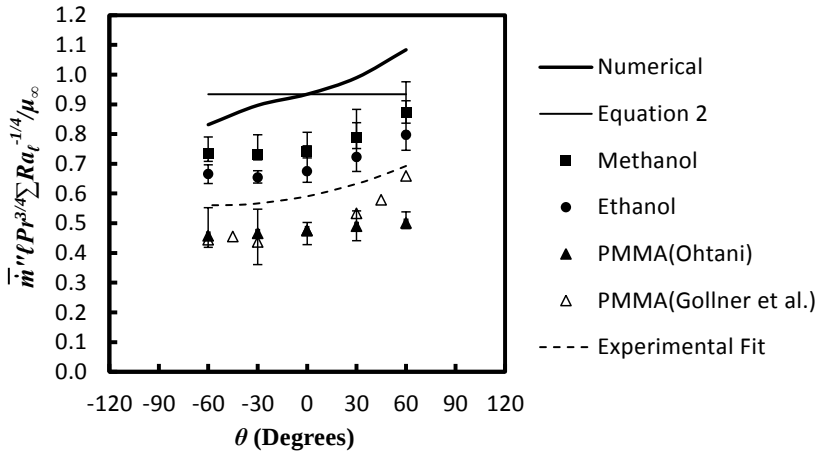

Figure 10. Dimensionless burning rate for the full set of data. Symbols indicate average burning rates with vertical bars indicating the variability. Equation 2, $\overline{\dot{m}''}\ell Pr^{\frac{3}{4}}\Sigma\, Ra_\ell^{*-\frac{1}{4}}/\mu_\infty = 0.934$ is derived from Ahmad and Faeth. Numerical calculation is based on modified equations from this study and a fit of experimental data is shown.

Based on all the experimental data presented in Fig. 10, an average fit was developed as a function of $\tan\theta$

$$\frac{\overline{\dot{m}''}\ell Pr^{3/4}\Sigma Ra_\ell^{*-1/4}}{\mu_\infty} = 0.0154(\tan\theta)^2 + 0.0399\tan\theta + 0.5953. \qquad (2d)$$

In the numerical study by Ali et al. [8], a fit by them of the effect of orientation gives a dependence very similar to our behavior in Fig. 10. This dashed curve in Fig. 10 follows the trend for each of the three fuels. However, another factor, perhaps radiation, is causing differences between fuels. The parameter $\sum$ is plotted as a function of B in Fig.

11. $\sum$ is calculated using property data for a range of materials given in Table 2. For non-charring materials ($B > 0.8$), a simpler expression for $\sum$ is found solely depending on B,

$$\Sigma = 1.6B^{-0.74}. \tag{2e}$$

Combining Eq. (2d) and (2e) leads to a functional relationship for the burning rate based solely on the B number and angle of inclination is

$$\frac{\overline{\dot{m}''}\ell Pr^{3/4}Ra_\ell^{*-1/4}}{\mu_\infty} = \frac{0.0154(\tan\theta)^2+0.0399\tan\theta+0.5953}{1.6B^{-0.74}}. \tag{2f}$$

This is a relative simple equation for plate burning rate. The parameter Ω is plotted in a similar way as a function of only B using Table 2. For non-charring materials, Ω remains nearly constant with a value of 0.3 for most of the materials. Thus, Eq. (1a) can be presented in a more simple form:

$$\left(\frac{y_f}{x}\right) Gr_x^{*1/4} = \frac{3.6}{0.3} = 12, \qquad \text{for } B > 0.8. \tag{2g}$$

Table 2. Estimated dimensionless properties including Ω and Σ.

Material	Δh_c^a (kJ/g)	L^a (kJ/g)	T_v^a (°C)	B^a	Ω^b	Σ^b
			Liquids			
n-Hexane	42	0.45	69	6.7	0.28	0.41
n-Heptane	41	0.48	98	6.2	0.28	0.43
n-Octane	41	0.52	125	5.7	0.27	0.44
Benzene	28	0.48	80	6.2	0.31	0.44
Toulene	28	0.50	110	5.9	0.31	0.45
Naphthalene	30	0.55	218	5.2	0.29	0.47
Methanol	19	1.2	64	2.5	0.36	0.8
Ethanol	26	0.97	78	3.1	0.31	0.67
n-Butanol	35	0.82	117	3.6	0.28	0.59
Acetone	28	0.58	56	5.2	0.4	0.6
			Solids			
Polyethylene	38	3.6	360	0.75	0.27	2.02
Polypropylene	38	3.1	330	0.89	0.27	1.72
Nylon	27	3.8	500	0.68	0.32	2.25
Polymethylmethacylate	24	2.0	300	1.4	0.31	1.2
Polystyrene	27	3.0	350	0.91	0.31	1.73
			Solids, charring			
Polyurethane foam, rigid	17	5.0	300	0.56	0.52	3.08
Redwood	12	9.4	380	0.29	3.62	8.26
Red oak	12	9.4	300	0.30	3.14	8.07
Maple	13	4.7	350	0.58	0.68	3.08

a. Quintiere, J. G., *Fundamentals of Fire Phenomena* [16]
b. Eq. 1b
c. Eq. 2c

MATHEMATICAL MODEL

Here the model of Ahmad and Faeth [6, 7] is considered, except now the pressure gradient of the normal momentum equation is included. This effect produces an additional buoyancy term that aligns with the main flow direction. It will be called "the cross-flow effect (CF)". This effect of the fuel surface is included to help differentiate between

burning at the top and the bottom for the same inclination. We wish to see if this inclusion explains the behavior of the correlations of Eq. (1) and (2) with the data. The following assumptions are taken into account in the development of the model:

- The ambient atmosphere has a constant temperature and composition.
- Density does not change strongly with *x*.
- The flame is laminar, two dimensional and steady.
- Boundary layer assumptions apply.
- The flow is a mixture of an ideal gas with a constant specific heat and unity Lewis number.
- Radiation and viscous dissipation are neglected.
- The combustion process is a single global chemical reaction.
- The flame sheet assumption is taken.

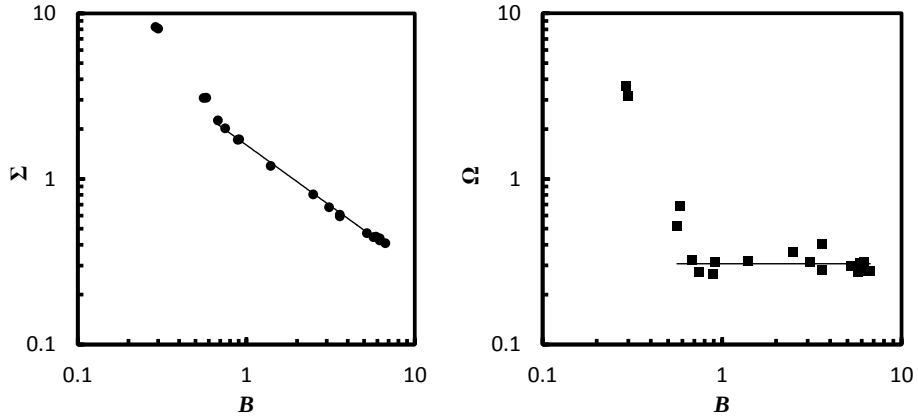

Figure 11. Dimensionless parameters fit as a function of *B*.

The pressure is decomposed into pertabation and static terms, $p = \tilde{p} + p_s$, where

$$\frac{dp_s}{dY} = -\rho_\infty g. \tag{3}$$

The coordinate system given in Fig. 9 may be written as $Y = x\cos\theta + y\sin\theta$ so that the pressure gradients in the *x* and *y* directions can be expanded into perturbation and buoyancy terms. Following these assumptions, the boundary layer equations,

$$\frac{\partial(\rho u)}{\partial x} + \frac{\partial(\rho v)}{\partial y} = 0 \tag{4}$$

$$\rho\left(u\frac{\partial u}{\partial x} + v\frac{\partial u}{\partial y}\right) = \frac{\partial}{\partial y}\left(\mu\frac{\partial u}{\partial y}\right) - \left(\frac{\partial \tilde{p}}{\partial x}\right)_y + (\rho_\infty - \rho)g\cos\theta \tag{5}$$

$$0 = -\left(\frac{\partial \tilde{p}}{\partial y}\right)_x + (\rho_\infty - \rho)g\sin\theta \tag{6}$$

$$\rho\left(u\frac{\partial \Phi}{\partial x} + v\frac{\partial \Phi}{\partial y}\right) = \frac{\partial}{\partial y}\left(\frac{k}{c_p}\frac{\partial \Phi}{\partial y}\right) + \dot{m}_f{}'''\Delta h_c \tag{7}$$

$$\rho\left(u\frac{\partial \mathrm{Y}_i}{\partial x}+v\frac{\partial \mathrm{Y}_i}{\partial y}\right)=\frac{\partial}{\partial y}\left(\rho D\frac{\partial \mathrm{Y}_i}{\partial y}\right)+\dot{m}_i{}''' \tag{8}$$

are written for the conservation of mass, momentum, energy and species, respectively, with enthalpy $\Phi = \int_{T_\infty}^{T} c_p dT \cong \bar{c_p}(T - T_\infty)$.

A one-step reaction is presented as the mass-based stoichiometric equation, 1 g Fuel + s g Oxygen ⇒ (1+s) g Product. The pressure is constant, so that the perfect gas theory gives $\rho T = \rho_\infty T_\infty$ or

$$\frac{\rho_\infty - \rho}{\rho} = \frac{T - T_\infty}{T_\infty} = \frac{\Phi}{c_p T_\infty}. \tag{9}$$

These compressible equations are transformed into an incompressible form by introducing the Howarth-Dorodnitzyn transformation [14] $z = \int_0^y \frac{\rho}{\rho_\infty} dy$, in which $z = z(x, y)$. Also, $\rho\mu$ is assumed to be constant.

The Shvab-Zel'dovich (S-Z) variables are introduced

$$\beta_{\Phi \mathrm{O}} = \Phi + \frac{\mathrm{Y}_o \Delta h_c}{s} \tag{10}$$

$$\beta_{\Phi \mathrm{F}} = \Phi + \mathrm{Y}_F \Delta h_c \tag{11}$$

$$\beta_{\mathrm{FO}} = \mathrm{Y}_F + \frac{\mathrm{Y}_o}{s}. \tag{12}$$

Furthermore, the Prandtl and Schmidt number are assumed to equal unity, $Pr = \frac{\mu c_p}{k} = 1$ and $Sc = \frac{\mu}{\rho D} = 1$. A dimensionless mixture fraction is introduced,

$$\beta^* = \frac{\beta_\mathrm{i} - \beta_{\mathrm{i},\infty}}{\beta_{\mathrm{i,w}} - \beta_{\mathrm{i},\infty}}, \tag{13}$$

in which "*w*" implies conditions at the wall, $y = 0, z = 0$; and ∞ implies ambient conditions, where $y \to \infty$ and $z \to \infty$.

The conservation equations then become:

$$L[u] = \left(\frac{\rho_\infty - \rho}{\rho}\right) g \cos\theta - \frac{1}{\rho}\left(\frac{\partial \tilde{p}}{\partial x}\right)_y, \tag{14}$$

where the operator *L* is $L \equiv u\frac{\partial}{\partial x} + w\frac{\partial}{\partial z} - \frac{\partial}{\partial z}(\rho\mu)\frac{\partial}{\partial z}$ and $w = \rho v + u\int_0^y \left(\frac{\partial \rho}{\partial x}\right)_y dy$.

The pressure gradient term in Eq. (14) can be expanded by the chain rule,

$$\begin{aligned}\left(\frac{\partial \tilde{p}}{\partial x}\right)_y &= \left(\frac{\partial \tilde{p}}{\partial x}\right)_z + \left(\frac{\partial \tilde{p}}{\partial z}\right)_x \left(\frac{\partial z}{\partial x}\right)_y \\ &= -\frac{\partial}{\partial x}\int_z^\infty \left(\frac{\rho_\infty - \rho}{\rho}\right) g \sin\theta \, dz + \left(\frac{\rho_\infty - \rho}{\rho}\right) g \sin\theta \int_0^y \left(\frac{\partial \rho}{\partial x}\right)_y dy.\end{aligned} \tag{15}$$

Invoking slow variation of density in the *x*-direction allows the assumption: $\left(\frac{\partial \rho}{\partial x}\right)_y \approx 0$, and $\rho \to \bar{\rho}$, a mean density. Then the operator over the velocity and mixture fraction becomes

$$L[u] = \left(\frac{\rho_\infty - \rho}{\rho}\right) g \cos\theta + \frac{g \sin\theta}{\bar{\rho}} \frac{\partial}{\partial x}\int_z^\infty \left(\frac{\rho_\infty - \rho}{\rho}\right) dz \tag{16}$$

with $L[\beta^*] = 0$. The second term on the right-hand side of Eq. 16, containing sinθ, is the "cross flow effect".

The boundary conditions follow as:

$$x = 0:\ u = 0, \beta^* = 0$$

$$z = 0:\ u = 0, \qquad \beta^* = 1, w = -\frac{\rho\mu}{\rho_\infty Pr} B \left(\frac{\partial \beta^*}{\partial z}\right)_{z=0}, \qquad \text{where } B = \frac{\frac{Y_{o,\infty}\Delta h_c}{s} - \Phi_w}{L},$$

$$z \to \infty:\ u = 0, \frac{\partial u}{\partial z} = 0 \quad \text{and} \quad \beta^* = 0, \frac{\partial \beta^*}{\partial z} = 0.$$

From the relationship between density, temperature and enthalpy, along with the definition of S-Z variable it can be shown that [6, 7]

$$\frac{\rho_\infty - \rho}{\rho} = \frac{L}{\bar{c_p} T_\infty}\left[\left(B + \frac{\Phi_w}{L}\right) - B\beta^*\right] \quad 0 \le \zeta \le \zeta_f \tag{17}$$

$$\frac{\rho_\infty - \rho}{\rho} = \frac{L}{\bar{c_p} T_\infty}\left(\frac{B + \frac{\Phi_w}{L}}{{\beta_f}^*} - B\right)\beta^* \quad \zeta_f \le \zeta \le 1 \tag{18}$$

$${\beta_f}^* = \left(\frac{B+1}{B}\right)\left(\frac{S}{S+1}\right), \zeta_f = 1 - {\beta_f}^{*1/3}, \qquad S \equiv \frac{Y_{o,\infty}}{s Y_{F,T}}, Y_{F,T} \equiv 1 \tag{19}$$

To facilitate an integral solution, the equations are integrated across the boundary layer to form ordinary differential equations

$$\frac{d}{dx}\int_0^\infty u^2 dz + \left(\frac{\mu_\infty}{\rho_\infty}\right)\left(\frac{\partial u}{\partial z}\right)_{z=0} = \int_0^\infty \left(\frac{\rho_\infty - \rho}{\rho}\right) g \cos\theta \, dz + \frac{g \sin\theta}{\bar{\rho}/\rho_\infty} \frac{d}{dx}\int_0^\infty z\left(\frac{\rho_\infty - \rho}{\rho}\right) dz \tag{20}$$

$$\frac{d}{dx}\int_0^\infty (u\beta^*) dz + \frac{\nu_\infty}{Pr}(B+1)\left(\frac{\partial \beta^*}{\partial z}\right)_{z=0} = 0 \tag{21}$$

in which $\frac{\rho\mu}{{\rho_\infty}^2} = \frac{\mu_\infty}{\rho_\infty} \equiv \nu_\infty$, the kinematic viscosity.

A new z-variable is introduced and profile functions are introduced for u and β,

$$\int_0^\infty dz \to \delta \int_0^1 d\zeta\,, \zeta \equiv \frac{z}{\delta}. \tag{22}$$

The profiles satisfy the natural boundary conditions above and the derived conditions,

$$\frac{\partial^2 u}{\partial z^2} = \text{function}(x), at\ z = 0$$

and

$$\frac{\partial^2 \beta}{\partial z^2} = 0\ at\ z \to \infty.$$

The resulting profiles follow from [6, 7],

$$u = u_0(x)\zeta(1-\zeta)^2 \text{ and} \tag{23}$$

$$\beta^* = (1-\zeta)^3. \tag{24}$$

Because the derived boundary condition on the velocity ignored mass transfer, a blowing correction term suggested by Marxman [15] as $\ln(1+\mathrm{B})/\mathrm{B}$ was included as a multiplying term for the diffusive transport terms at the wall. The equations become

$$\left(\int_0^1 \zeta^2(1-\zeta)^4 d\zeta\right)\frac{d({u_0}^2\delta)}{dx} + \gamma_\infty \frac{\ln(1+B)}{B}\frac{u_0}{\delta} = g\cos\theta\,\delta\int_0^1\left(\frac{\rho_\infty-\rho}{\rho}\right)d\zeta + \frac{g\sin\theta}{\bar{\rho}/\rho_\infty}\left[\int_0^1\left(\frac{\rho_\infty-\rho}{\rho}\right)\zeta d\zeta\right]\frac{d(\delta^2)}{dx} \tag{25}$$

and

$$\left(\int_0^1 \zeta(1-\zeta)^5 d\zeta\right)\frac{d(u_0\delta)}{dx} + (-3)\frac{\nu_\infty}{Pr}\frac{(B+1)}{\delta}\frac{\ln(1+B)}{B} = 0. \tag{26}$$

Introducing dimensionless variables as $\xi = \frac{x}{l}, U = \frac{u_0\delta}{\nu_\infty}, \Delta = \frac{\delta}{l}$ gives

$$\frac{1}{105}\frac{d(U^2\Delta)}{d\xi} + \frac{\ln(1+B)}{B}\frac{U}{\Delta} = \left(\frac{g\cos\theta\,L}{4\bar{c_p}T_\infty}\frac{l^3}{{\nu_\infty}^2}\right)\left(a\Delta + \frac{b\tan\theta}{\bar{\rho}/\rho_\infty}\frac{d\Delta^2}{d\xi}\right) \tag{27}$$

$$\frac{1}{42}\frac{d(U\Delta)}{d\xi} - \frac{3(B+1)}{Pr}\frac{\ln(1+B)}{B\Delta} = 0 \tag{28}$$

with

$$a \equiv 3(B+\tau_0)\zeta_f + \tau_0, \tag{29a}$$

and

$$b \equiv \left(\frac{B+\tau_0}{S}\right)\left(6{\zeta_f}^2 + 3\zeta_f + 1\right) - \frac{B}{5}, \tau_0 = \frac{\Phi_w}{L} = \frac{\bar{c_p}(T_w - T_\infty)}{L}. \tag{29b}$$

Using initial condition $\xi = 0, U = \Delta = 0$, solutions for U and Δ with regard to ξ can be found. The term containing b above is the cross flow effect. When b = 0, the analytical solutions given in Eq. (1) and (2) can be found, otherwise a numerical solution must be rendered.
The burning rate and the flame standoff distance can be formulated as follows:

The local burning rate is

$$\frac{\dot{m}_F'' l}{\mu_\infty} = \frac{3}{Pr}\frac{\ln(1+B)}{\Delta}, \tag{30}$$

the average burning rate is

$$\frac{\overline{\dot{m}_F}'' l}{\mu_\infty} = \frac{3}{Pr}\ln(1+B)\int_0^1\frac{d\xi}{\Delta} \tag{31}$$

and the flame standoff distance is

$$y_f = c\Delta l, \text{with } c \equiv \left(\frac{L}{4\bar{c_p}T_\infty}\right)\left[4(B+\tau_0)\zeta_f + B\left[\left(1-\zeta_f\right)^4 - 1\right]\right] + \zeta_f. \tag{32}$$

For b = 0, by which the cross-flow effect is neglected, the equations are solved analytically as done previously by Ahmad and Faeth [6, 7] giving

$$U = \left[\frac{168a(1+B)Gr_l^*}{2(1+B)+Pr}\right]^{\frac{1}{2}}\xi^{\frac{1}{2}} \tag{33}$$

$$\Delta = \left[\frac{\ln(1+B)}{BPr}\right]^{\frac{1}{2}}\left[\frac{168(1+B)[2(1+B)+Pr]}{Gr_l^* * a}\right]^{\frac{1}{4}}\xi^{\frac{1}{4}} \tag{34}$$

in which $$Gr_l^* = \frac{g\cos\theta\,L}{4\bar{c_p}T_\infty}\frac{l^3}{{\nu_\infty}^2}.$$

Substituting U and Δ into the burning rate and flame standoff distance gives Eqns. (1) and (2).

For the *b* term not equal to zero, the equations are solved numerically using *Mathematica*. Due to singularity issues near the origin, the solution was problematic and is only solved for limited cases. The results of the experiments will be compared to solutions with and without the cross flow term.

Figure 11 shows the results of the theory compared to methanol data of 10 cm in length. Little difference is found from the theoretical result with and without the cross flow effect. Also, the results vary little with angle, and the flame standoff distance is again over-predicted, especially for burning on the underside. Moreover, the steady laminar theory does not fully apply.

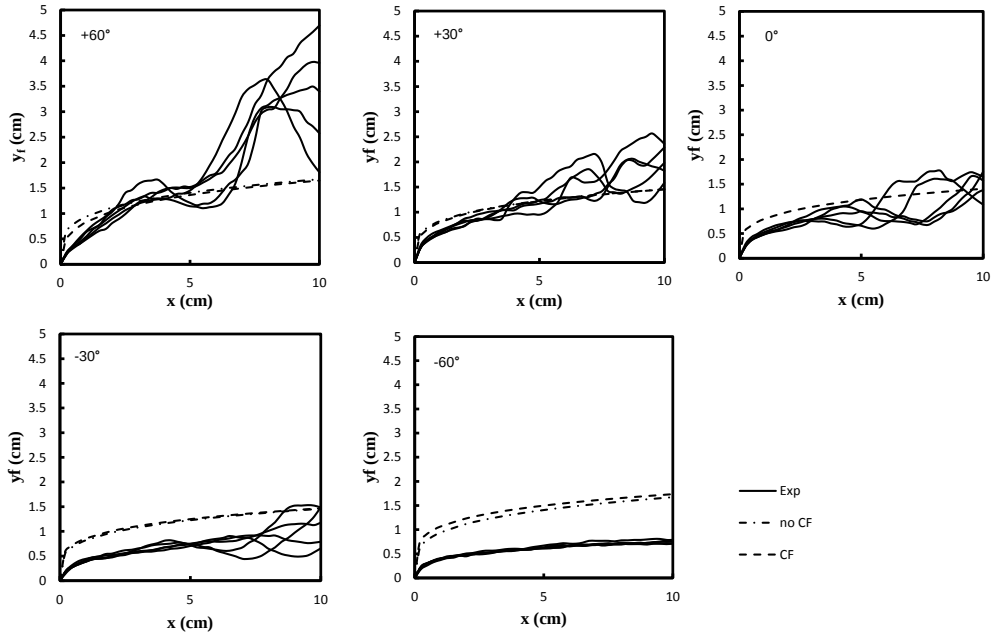

Figure 11. Comparison of theoretical and experimental instantaneous results for flame standoff with methanol of l = 10 cm

Figure 12 shows the burning rate per unit area results for ethanol and methanol. The burning rate is higher for top burning at corresponding orientations than burning on the underside with the cross flow term (CF) included. Without CF, the results are symmetrical. The CF results better agree with the data of Figure 6, and support the increase in burning rate with angle as depicted in Figure 10.

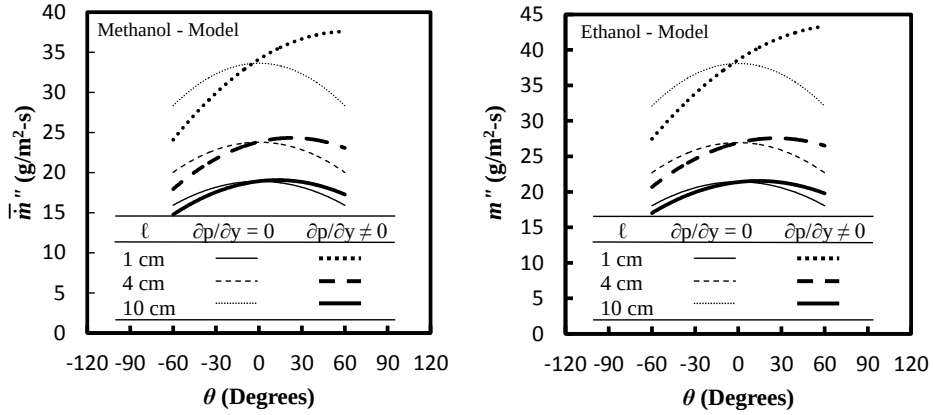

Figure 12. Theoretical results for average burning flux for methanol and ethanol

CONCLUSIONS

Measurements of flame location and burning rate were recorded for flat plate wicks of methanol and ethanol, ranging in size from 1 to 10 cm, and oriented from 0º (vertical) to +/- 90º (top/bottom). The dimensionless laminar correlations of Ahmad and Faeth [6, 7] roughly support the data for flame location and burning flux, however the flame location is over predicted, and indicates no additional dependence on the angle. In contrast, the results for the burning rate indicate increasing rates with angle. In addition, there is a maximum burning rate at + 30º whose location with angle appears to decrease as the length of the plate increases. While the theory only considers laminar steady pure convection, issues related to the onset of turbulence and radiation is present. The inclusion of the cross flow, or normal pressure term, in the theory gives improved results, especially in predicting the differences in the top and bottom burning rate for the same plate orientation. Simple fits for mass burning rates and flame standoff, equations (2f) and (2g) were formed based on the theory which include dependence on the Grashof number, *B* number and angle.

ACKNOWLEDGMENTS

The authors would like to thank M. Huis, M. Lutz, and M. Willnauer for their contributions. This work was supported by a NASA Office of the Chief Technologist's Space Technology Research Fellowship (NASA Grant NNX11AN68H with grant monitor D. Urban). This work was also funded by NASA Grant NNX10AD98G, with P. Ferkul as technical contact.

REFERENCES

1. Blackshear Jr., P.L. and Murty, K.A., "Heat and mass transfer to, from, and within cellulosic solids burning in air," Symposium (Intl.) on Combustion 10: 911-923 (1965).
2. Blackshear Jr., P.L. and Murty, K.A., "Some effects of size, orientation, and fuel molecular weight on the burning of fuel-soaked wicks," Symposium (Intl.) on Combustion 11: 545-552 (1967).
3. Kosdon, F.J., Williams, F.A. and Buman, C., "Combustion of vertical cellulosic cylinders in air," Symposium (Intl.) on Combustion 12: 254-264 (1969).
4. Kim, J.S, de Ris, J. and Kroesser, William F., "Laminar free-convective burning of fuel surfaces," Symposium (Intl.) on Combustion 13: 949-961 (1971).
5. Orloff, L. and de Ris, J., "Modeling of Ceiling Fires," Symposium (Intl.) on Combustion 13: 979-992 (1971).
6. Ahmad, T. and Faeth, G.M., "Turbulent wall fires," Symposium (Intl.) on Combustion 17: 1149-1160 (1979).
7. Ahmad, T., "Investigation of the Combusting Region of Fire-Induced Plumes Along Upright Surfaces," Ph.D. Thesis, The Pennsylvania State University, 1978.
8. Ali, S., Raghavan, V.and Rangwala, A., "A numerical study of quasi-steady burning characteristics of a condensed fuel: effect of angular orientation of fuel surface," Combustion Theory and Modeling 14, No. 4: 495-518 (2010).
9. Ohtani, H., Ohta, K. and Uehara, Y., "Effect of orientation on burning rate of solid combustible," Fire and Materials 18: 191-193 (1991).
10. Gollner, M.J., Huang, X., Cobian, J., Rangwala, A.S. and Williams, F.A, "Experimental study of upward flame spread of an inclined fuel surface," Proceedings of the Combustion Institute 34: 2531-2538 (2013).
11. Lloyd J.R., Sparrow E.M., "On the Instability of natural convection flow on inclined plates," Journal of Fluid Mechanics, No. 42, pp. 465-470 (1970).
12. Al-Arabi, M. and Sakr, B., "Natural convection heat transfer from inclined isothermal plates," International Journal of heat and Mass Transfer, 31: 559–566 (1988).
13. Bustamante, M., "Experimental Investigation Of Liquid And Gas Fueled Flames Towards The Development Of A Burning Rate Emulator (BRE) For Microgravity Applications", Master of Science Thesis, Dept. of Fire Protection Engineering, University of Maryland, College Park, MD 20742, 2012.
14. Howarth, L., "Concerning the effect compressibility on laminar boundary layers and their separation," Proc. Roy. Soc. London Ser. A 194: 16-42 (1948).
15. Marxman, G., Gilbert, M., "Combustion in the Turbulent Boundary Layer on a Vaporization Surface," Symposium (Intl.) on Combustion 10: 1337-1349 (1965).
16. Quintiere, J.G., *Fundamentals of Fire Phenomena*. John Wiley & Sons Ltd., Chichester, UK, 2006.